actuators

MDPI

Article

UKF-Based Observer Design for the Electric Brake Booster in Situations of Disturbance

Mingming Mei [1,*], Shuo Cheng [2,*], Liang Li [1], Hongyuan Mu [1] and Yuxuan Pei [1]

[1] State Key Laboratory of Automotive Safety and Energy, Tsinghua University, Beijing 100084, China
[2] The Institute of Industrial Science, University of Tokyo, Tokyo 153-0041, Japan
* Correspondence: mmm19@mails.tsinghua.edu.cn (M.M.); shuocheng9@yeah.net (S.C.)

Abstract: The motor-driven electric brake booster (E-Booster) can replace the traditional vacuum booster to realize the braking power assistance and active braking. Independent of extra sensors, this paper proposes a full-state observer for E-Booster based on Unscented Kalman Filter (UKF) in the presence of a driver's input force disturbance. The electro-hydraulic system is first modeled, which includes a nonlinear hydraulic model and the reaction disk's rubber model. The pre-compression is designed to produce linear power assistance based on the properties of rubber material. With the existence of the disturbance, the linear quadratic regulator (LQR) algorithm is used to track the pre-compression of the reaction disk so that E-Booster is developed into a closed-loop system to achieve power assistance. The proposed UKF observer can online estimate the states considering the controller input and disturbance input. To reduce the process error, the hydraulic p-V characteristic is fitted using the recursive least squares (RLS) method before observation. Furthermore, the simulation test and vehicle tests are performed to validate the observation effect. In the closed-loop test, UKF decreases residual error by 16% when compared to the typical Extended Kalman Filter (EKF). The simulation results remain consistent with the experimental results, demonstrating the effectiveness of the proposed method.

Keywords: E-Booster; power assistance; pre-compression of the reaction disk; UKF; RLS estimator; LQR

Citation: Mei, M.; Cheng, S.; Li, L.; Mu, H.; Pei, Y. UKF-Based Observer Design for the Electric Brake Booster in Situations of Disturbance. *Actuators* **2023**, *12*, 94. https://doi.org/10.3390/act12030094

Academic Editors: Bobo Helian and Zheng Chen

Received: 2 February 2023
Revised: 13 February 2023
Accepted: 16 February 2023
Published: 22 February 2023

1. Introduction

X-by-wire actuators have been fully developed and are gradually becoming the standard actuator scheme due to the civil application of electric vehicles. Electric brake booster (E-Booster), which decouples pedal force from wheel cylinder pressure via a motor, outperforms conventional actuators based on servo valves or high-pressure accumulators. Its benefits include: (1) decreased space, weight, and cost [1,2]; (2) increased adjustable bandwidth and improved robustness [1]; (3) the ability to reconcile the cooperative energy regeneration with braking [3]; and (4) higher reliability and fault tolerance [4], wherein identifying performance features is critical for product adaption and fault diagnosis.

In the practical application of active braking technology, identification of key characteristics is necessary. The behavior of the closed-loop system can be predicted using key state estimation, which is important for the state-feedback based controller. However, in the presence of disturbance or measurement errors, the prediction purely based on the model is partial and inaccurate. As a key component of Model Predictive Control (MPC), the literature [5–7] devised several nonlinear observers to estimate the state variables. Furthermore, characteristic curves comprising measurable and unmeasurable states can characterize system performance. These applications are not just for the controller's design stage. The observer signal could also be employed for fault diagnosis [8,9] by residual evaluation. As for the E-Booster, the pedal force vs. pressure or pushrod displacement curves, in general, represent the boost characteristics; meanwhile, the pushrod displacement vs.

pressure curve reflects E-Booster hydraulic characteristics. However, some of these signals are either impossible to measure or improper for measurement. For example, E-Booster has no space for extra sensors to directly measure the pushrod displacement or speed, and the pedal force sensor does not exist due to high cost. It is valuable to propose an identification method to estimate the key state.

To improve the observation accuracy of the model, the offline data set is used to fit the hydraulic system's characteristics. Some studies characterized the system by a specific model based on the gathered data under the predesigned excitation signal. To begin, essential state information would be extracted from the system model, which had been extensively explored by several researchers. Hong conducted a state variable filter [10] to generate key kinematic variables, and a state estimate module was created specifically for sensor signal fusion [11]. After that, an optimization approach, such as the RLS method [10,12,13] or a parameter estimator based on the observer [14], would be used to solve the parameters of the constructed model.

The observers based on KF (Kalman Filter) have been frequently used in engineering because they can efficiently solve the process and measurement noise [15]. However, since KF is valid only for linear space, a better solution is required for the nonlinear problem. Ref. [16] proposed a UKF (Unscented Kalman Filter) based motor torque diagnosis algorithm to estimate the fault parameter. The prior system and measurement noise were both used, and results were satisfactory. Some researchers considered the noise as the posterior and added another KF to estimate the covariance. Lee et al. demonstrated that the dual KF had high convergence performance in parameter estimation [17], and the constrained vehicle parameters could be updated in real time by the dual KF [18]. In addition, the literature [19] recommended an adaptive technique to obtain the suitable covariance matrix for the constrained UKF.

To the best of our knowledge, few previous studies have focused on the full-state observation of E-Booster system in the presence of driver's input force disturbance. Full-state observations obtain more comprehensive information and have the following advantages. First, the full-state observation facilitates the design of some controllers, such as LQR, MPC, etc. In addition, some intermediate quantities are artificially set when describing the nonlinear characteristics of the feedback disk and hydraulics. It can not be measured directly by the sensor, but only by the observer. Therefore, this paper proposes an UKF-based state observer for recognizing states, which aids in model prediction and fault diagnosis. During the build process of the observer, the dynamics of reaction disk and nonlinear hydraulic system are introduced to the mathematical model. The observer is constructed on a leverage-like concept with the purpose of the power-assisted process. The pre-compression of the reaction disk is presented for the linear power assistance, and an LQR controller is used for the closed-loop position tracking. During the design of UKF, RLS can estimate the hydraulic p-V characteristics to reduce the model observation error. In addition, the disturbance is described by chi-square distribution to facilitate the implementation of UKF based on Gaussian distribution. The suggested method can effectively estimate full state of the electro-hydraulic system and realize the online monitoring and state feedback control.

The following is how the rest of the paper is organized: In Section 2, the electro-hydraulic coupling and reaction disk models are created. Then, in Section 3, an identification technique based on UKF considering the disturbance is proposed. To demonstrate the effectiveness, simulation and experimental results are presented. Finally, the conclusions are given in Section 5.

2. Modeling

2.1. Electro-Hydraulic Coupling Model

The electro-hydraulic coupling actuator, which consists of a permanent magnet synchronous motor (PMSM), a reducer, and a master cylinder, is the subject of this study (see Figure 1). A two-stage gear reducer and a screw nut are used in the transmission mechanism to amplify the motor-driven torque and convert rotation into linear movement.

The motor load is the result of the superposition of a dynamic torque and a static torque, as follows:

$$T_L = T_S + T_D \tag{1a}$$

$$T_S = \frac{F_{op} l z_1 z_3}{2\pi z_2 z_4 \eta} \tag{1b}$$

$$T_D = J_e \ddot{\theta} \tag{1c}$$

where T_L, T_S, and T_D are the load torque, the static torque, and the dynamic torque. F_{op} is the force acting on the pushrod; η is the mechanical transmission efficiency; θ is the mechanical angle of PMSM; J_e is the equivalent inertia of the whole transmission mechanism; and the equation used to calculate J_e is presented as follows:

$$J_e = \frac{1}{2} m_1 r_1^2 + \frac{1}{2} m_2 r_2^2 \frac{z_1^2}{z_2^2} + \frac{1}{2} m_3 r_2^2 \frac{z_1^2}{z_2^2} + \frac{1}{2} m_4 r_4^2 \frac{z_1^2 z_3^2}{z_2^2 z_4^2} + \frac{1}{4\pi^2} m_5 l^2 \frac{z_1^2 z_3^2}{z_2^2 z_4^2} \tag{2}$$

where m_1, m_2, and m_3 are the mass of 1st, 2nd, and 3rd gears, respectively. m_4 is the sum of the mass of the 4th gear and nut. m_5 is the mass of the screw and output pushrod. r_1, r_2, r_3, and r_4 are the radii of each gear. z_1, z_2, z_3, and z_4 are the number of the teeth of each gear. l is the lead of the screw.

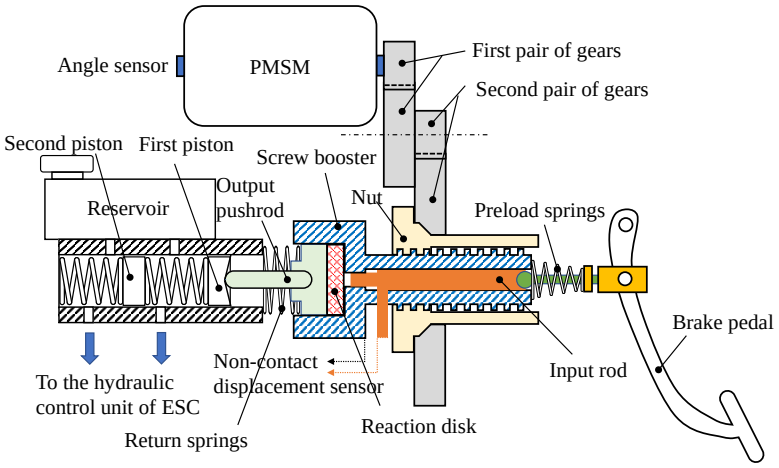

Figure 1. The structure diagram of the E-Booster.

The hydraulic component of the E-Booster is a series dual-chamber brake master cylinder in Figure 2. Motions of the two pistons are both considered when constructing the dynamic hydraulic model [20]. The following are the model equations:

$$\begin{cases} \dot{p}_m = \dfrac{E_m}{V_m - A_{mc} x_p} (A_{mc} \dot{x}_p - q_f - q_r) \\ \dot{p}_f = \dfrac{E_w}{V_f} q_f \\ \dot{p}_r = \dfrac{E_w}{V_r} q_r \end{cases} \tag{3}$$

$$q_{f,r} = C_q A \sqrt{\frac{\left| p_{f,r} - p_m \right|}{\rho}} \tag{4}$$

Without considering the action of the electro-magnetic valve, the remaining terminal hydraulic system, with the exception of the master cylinder, can be regarded as an airtight container whose properties can be represented by the p-V curve.

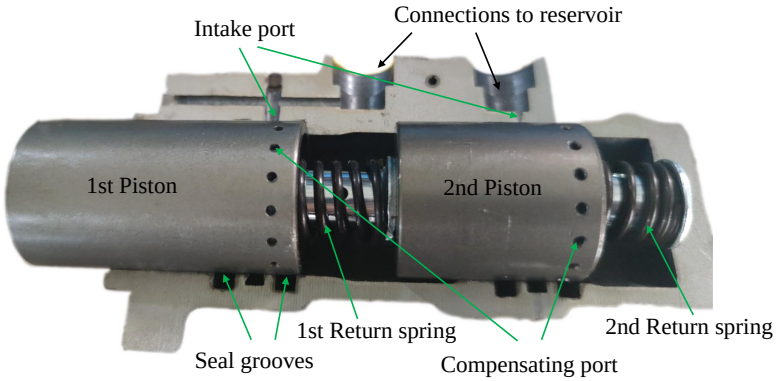

Figure 2. Half-cutaway view of the master cylinder.

2.2. Reaction Disk Model

The generalized Maxwell (GM) and Berg models are applied to fit characteristics of the reaction disk model. The viscoelastic property can be appropriately modeled by GM model, which consists of the elastic and damping forces [21], while the Berg model is a convenient method for shaping the friction with a compromise between accuracy and computation [22].

It is a universally accepted method to model the rubber material by a sequence of springs, dampers, and frictional elements (as seen in Figure 3c). The viscoelastic part is described by a GM with a nonlinear spring, while the frictional component uses the Berg model.

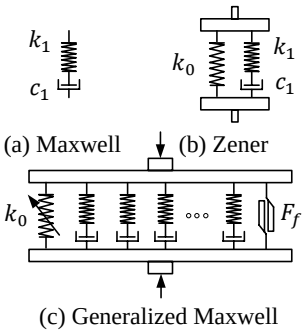

Figure 3. The schematic diagram of rubber models.

A single Maxwell model is the series connection between a spring and a damper (see Figure 3a). In addition, the Zener model can be thought as a spring element deposited with a Maxwell component (see Figure 3b). Hence, the GMM is also acknowledged as the Maxwell–Zener model.

Ignoring the influence of time-temperature superposition, differential equations reflecting the dynamic characteristics of the proposed model are presented as [23]

$$Maxwell: \ \dot{\sigma} + \frac{k_1}{c_1}\sigma = k_1\dot{\varepsilon} \tag{5a}$$

$$Zener: \ \dot{\sigma} + \frac{k_1}{c_1}\sigma = (k_0 + k_1)\dot{\varepsilon} + \frac{k_0 k_1}{c_1}\varepsilon \tag{5b}$$

where σ is the viscoelastic stress; ε is the viscoelastic strain.

The complex modulus of the models, which represents the ratio of loss to storage modulus, can be expressed as

$$Maxwell: \ k^*(\omega) = k_1 \frac{i\omega t_r}{1 + i\omega t_r} \tag{6a}$$

$$Zener: \ k^*(\omega) = k_0(x_{rd}) + k_1 \frac{i\omega t_{r1}}{1 + i\omega t_{r1}} \tag{6b}$$

$$GeneralizedMaxwell: \ k^*(\omega) = k_0(x_{rd}) + \frac{1}{k_0(x_{rd})} \sum_{j=1}^{n} k_j \frac{i\omega t_{rj}}{1 + i\omega t_{rj}} \tag{6c}$$

where $t_{rj} = c_j/k_j$, k_0 is the nonlinear spring stiffness of GM and $k_0 = \left.\frac{\partial F_0}{\partial x_0}\right|_{x_0 = x_{rd}}$.

In the quasi-static condition, the nonlinear relationship between the force and deformation can be fitted by the polynomial as follows [23]:

$$F_0 = 6D_{30}{x_{rd}}^5 + 4D_{20}{x_{rd}}^3 + 2D_{10}x_{rd} \tag{7}$$

where D_{30}/D_{10} and D_{20}/D_{10} are the constants.

When the uniaxial compressive deformation takes place, the quasi-static stiffness is damaged and will be recovered after a long time. The recovery process is described by an exponential damping function

$$D_{10} = D_{10-intrinsic} + (D_{10-damage} - D_{10-intrinsic})e^{-k_D t} \tag{8}$$

where $D_{10-intrinsic}$ is the intrinsic value when the reaction disk stays in a free state for long enough. $D_{10-damage}$ is every beginning value when the reaction disk just finished a compression. k_D is the fitted parameter, and t is the time since the last compression.

The deformation vs. force curve can reflect the quasi-static behavior of reaction disk (as seen in Figure 4). The behavior of reaction disk approaches the intrinsic behavior with the attenuation of D_{10}. The proposed nonlinear GM model method can fit the rubber material characteristics.

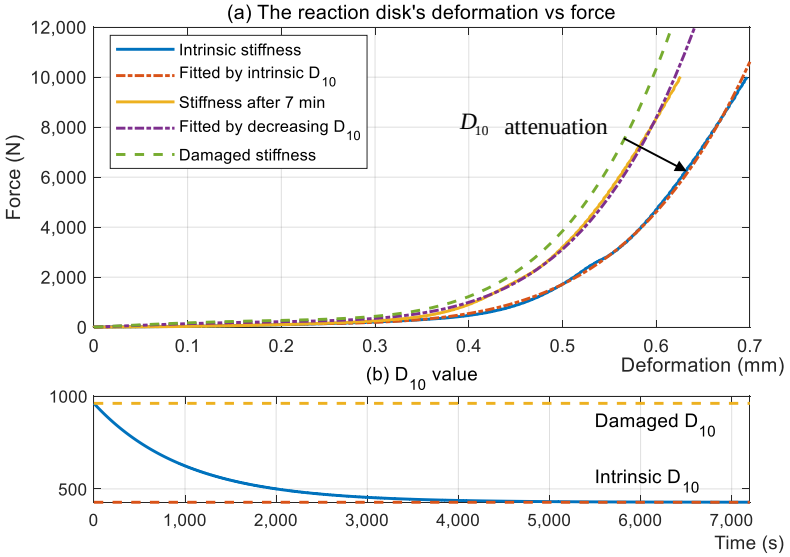

Figure 4. The quasi-static behavior of the reaction disk.

The Berg model is available for one-dimensional rubber material, and it has the advantage of balancing the connection between accuracy and computation [22]. In this research, just the internal friction among the three forces described by the Berg model has been considered. To avoid repetition, the remaining elastic and viscous forces will not be shown.

This model holds that the rubber's friction force depends on the deformation [24], and the friction can be calculated using the following equation:

$$F_f = \begin{cases} F_{fs} + \dfrac{x - x_s}{x_2(1-\alpha) + (x - x_s)}(F_{f\max} - F_{fs}), & x > x_s \\ F_{fs}, & x = x_s \\ F_{fs} + \dfrac{x - x_s}{x_2(1+\alpha) - (x - x_s)}(F_{f\max} + F_{fs}), & x < x_s \end{cases} \tag{9}$$

where $\alpha = F_{fs}/F_{f\max}$, and F_{fs} is the reference friction force. $F_{f\max}$ is the maximum friction force. x_s is the reference displacement that determines the property of the friction versus displacement graph with F_{fs}.The creep and relaxation behavior of proposed GM model is seen in Figure 5. There is the elastic deformation before the creep. It is more obvious for the deformation creep phenomenon in the return than the compression process. On the other hand, Figure 5 shows that the stress is gradually released to the steady state. The model can reflect both the creep and relaxation function, which has a direct influence on the final controlled effect.

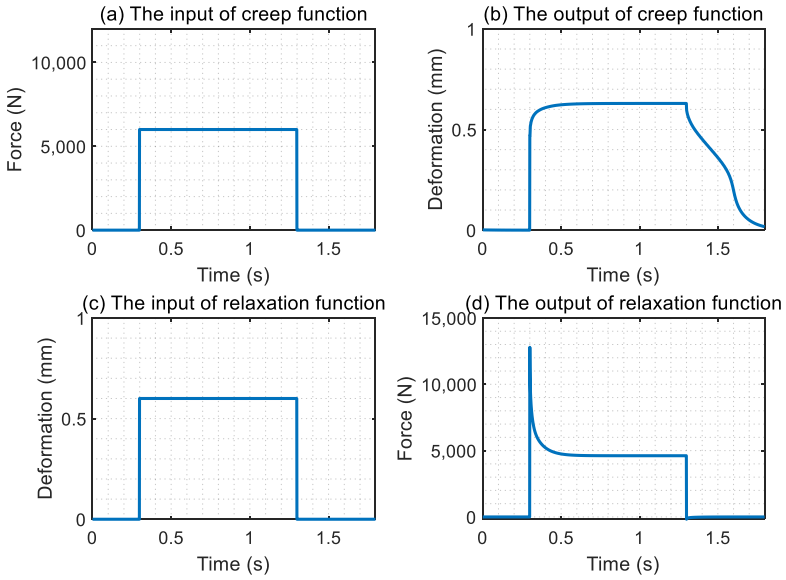

Figure 5. Creep and relaxation behavior.

2.3. Pre-Compression Strategy Based on the Leverage Model

Figure 6 illustrates the E-Booster's dynamic structure analogous with the leverage [25,26]. The input force and motor force can be equivalent to the forces on the leverage with the same direction. According to the leverage model, F_{servo} can be given by

$$\begin{cases} m_p\ddot{s} = F_{servo} + F_{in} - p_{mc}A_{mc} - k_r s \\ \dfrac{A_1}{A_2} \cdot \delta = G_{Rd1}(F_{in}) - G_{Rd2}(F_{servo}) \end{cases} \tag{10}$$

where s is the displacement of the piston, which can be approximately replaced by s_2. m_p is the piston mass. k_r is the stiffness of the return spring. δ is the relative compression between the surface A_1 and surface A_2 (seen in Figure 6). G_{Rd1}, G_{Rd2} are the transfer function from the stress to strain.

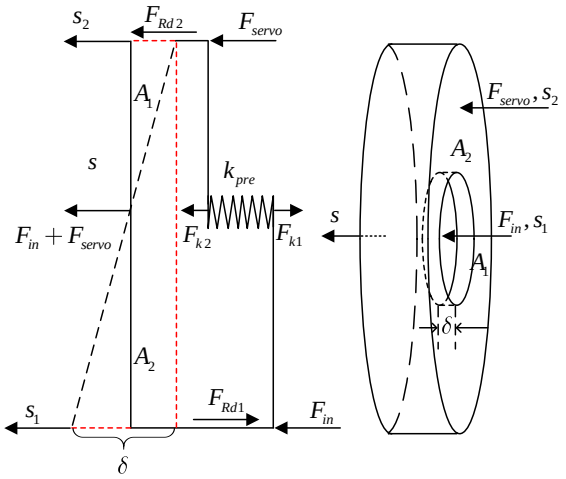

Figure 6. E-Booster kinematic model.

The target of this actuator is to realize the proportional amplification of the input force. The proportionality coefficient is predesigned relying on the driver preference. The reference signal δ_{ref} is the control objective in the following sections. The relationship between them can be seen in Figure 7. The input force F_{in} increases from 0 to 1000 N at a constant rate of 100 N/s. As the input force rises, the deformation difference between the surface A_1 and A_2 is increasing first and then decreasing gradually. The curve moves to the negative direction of the y-axis when the boost ratio is enlarged (the positive is the direction of pressure buildup). To keep the linearity of pedal feel, the input force is directly proportional to the screw booster displacement s_2. The reference deformation difference is designed according to the boost ratio as seen in the lower figure in Figure 7. Because the quasi-static behavior of the reaction disk is damaged after being squeezed by the stress, which is described in Equation (8), the real boost ratio is smaller than the predicted. The target curve of δ is adjusted downward, which is guaranteed within the limits of the reaction disk to avoid permanent damage to the rubber material's characteristics.

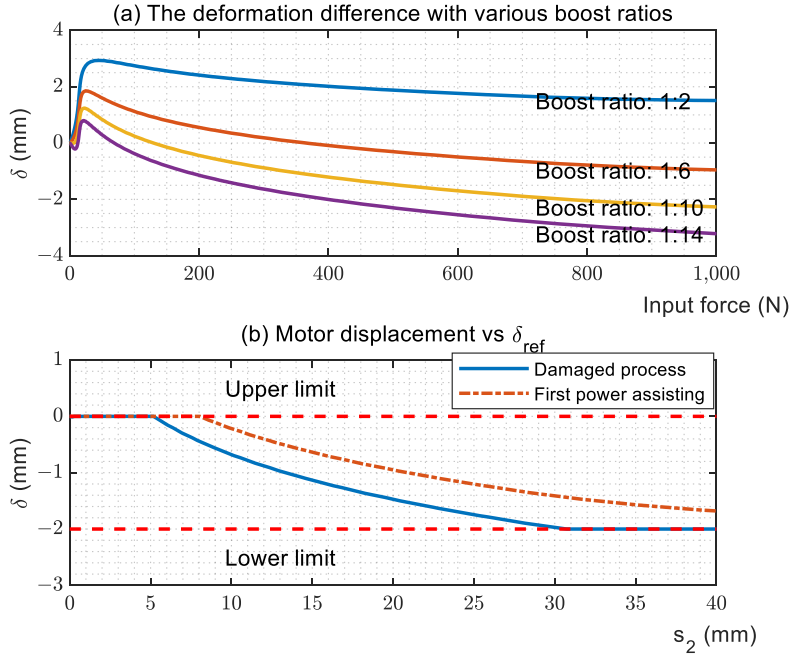

Figure 7. The target delta according to the boost ratio.

In Figure 6, the screw booster displacement s_2 is the input signal and the surface distance δ is the output. The linearized model at time t is displayed as follows:

$$\begin{cases} \dot{x} = A(t)x + B(t) \cdot \begin{bmatrix} s_2 & F_{in} \end{bmatrix}^T \\ y = C(t)x \end{cases} \tag{11}$$

where $x = \begin{bmatrix} p_m & p_f & p_r & \xi_1 & \xi_2 \end{bmatrix}^T$; p_m is the average pressure of the master cylinder; p_f and p_r are the circuit pressure linked to the front and rear chambers of the master cylinder; ξ_1 and ξ_2 are the state variables of the 2nd order transfer function for fitting reaction disk.

3. Closed-Loop Observation Algorithm Design

3.1. RLS p-V Characteristic Estimator

The training data are obtained when the screw booster maintains a constant speed to realize the increasing and decreasing of pressure. The pressure signal can be directly measured by a pressure sensor of the master cylinder, and the volume is converted by the displacement. The displacement vs. pressure curve is used to express the hydraulic p-V characteristics.

The polynomial fitting curve goes through the origin of coordinates, which can be obtained by the RLS with the forgetting factor as follows:

$$\varepsilon(k) = y_{RLS}(k) - w^H(k)x_{RLS}(k) \tag{12a}$$

$$k_{RLS}(k) = \frac{P_{RLS}(k) \cdot x_{RLS}(k)}{\lambda + {x_{RLS}}^H(k)P_{RLS}(k)x_{RLS}(k)} \tag{12b}$$

$$P_{RLS}(k+1) = \frac{1}{\lambda}\left[P_{RLS}(k) - k_{RLS}(k){x_{RLS}}^H(k)\ P_{RLS}(k)\right] \tag{12c}$$

$$w(k+1) = w(k) + k_{RLS}(k) \cdot \varepsilon^*(k) \tag{12d}$$

where ε is the estimation error, which is the exit condition for the iterations. y_{RLS} is the expected signal, namely the pedal force. x_{RLS} is a linear sequence related to the piston displacement (s_1 in Figure 6), such as $x_{RLS} = \begin{bmatrix} s_1^2 & s_1^4 & s_1^6 & s_1^8 \end{bmatrix}$. w is the FIR weighting coefficient. P_{RLS} is the recursive matrix with the initial value of δI ($0 < \delta \ll 1$). λ is the forgetting factor, and the value usually ranges from 0.9 to 1.

When s_1 is approximately replaced by s_2, Equation (3) can be written in the following nonlinear form:

$$\begin{cases} \dot{p}_m = \dot{f}_{RLS}(s_2) \\ \dot{p}_f = \dfrac{E_w C_q A}{V_f}\sqrt{\dfrac{\left|p_m - p_f\right|}{\rho}} \\ \dot{p}_r = \dfrac{E_w C_q A}{V_r}\sqrt{\dfrac{|p_m - p_r|}{\rho}} \end{cases} \tag{13}$$

3.2. Linearization

Taking the average curve of reaction disk in Figure 7, the force vs. deformation curve can be fitted by a piecewise continuous linear function. The triple piecewise function passes through the ordinate origin, which contains five coefficients to be solved. The triple piecewise function is as follows:

$$f(p, x_{train}) = \min\begin{pmatrix} p_3 x_{train}, \\ p_4 x_{train} + p_3 p_1 - p_4 p_1, \\ p_5 x_{train} + p_4 p_2 - p_5 p_2 \\ + p_3 p_1 - p_4 p_1 \end{pmatrix} \tag{14}$$

where p_1 and p_2 are the x-coordinate of the breakpoint; p_3, p_4, p_5 are the partial slope.

The solver adopts the trust region reflective method, which transfers the optimal problem to a series of easier local optimal problems [27]. The fitting results are shown in Figure 8.

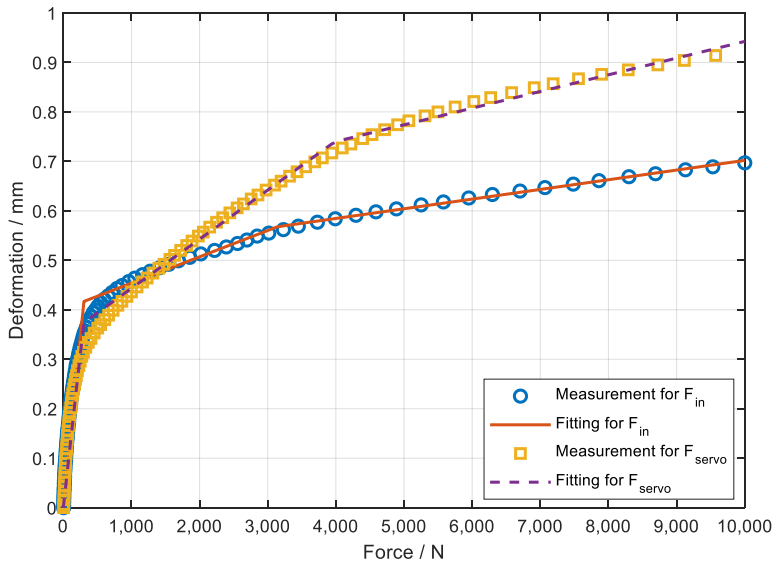

Figure 8. Piecewise fitting for quasi-static behavior.

The dynamic behavior is fitted by a second-order transfer function with two poles and one zero. The normalized transfer function is described in Figure 9.

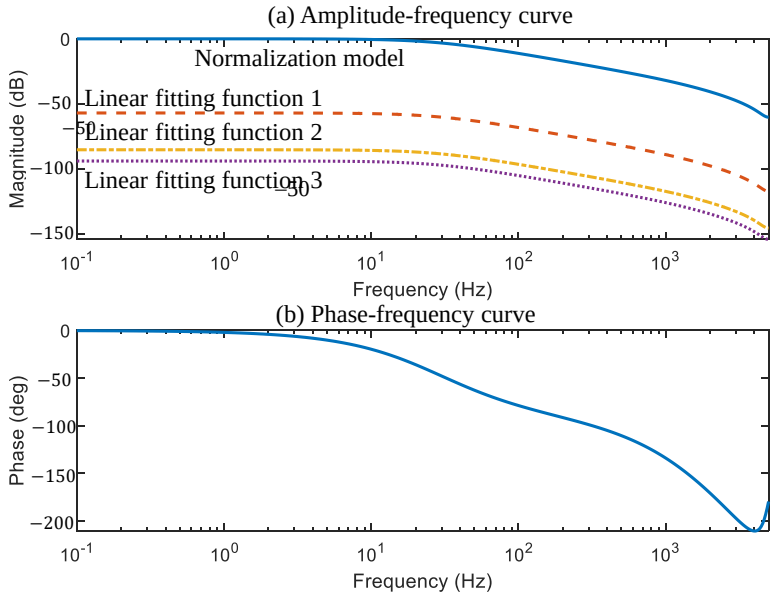

Figure 9. The fitted model for dynamic behavior.

Connected with Equation (14), the linear time-varying model Equation (11) is reached after linearization at time t.

3.3. Design of the Controller

For the design of the controller, the driver's input force is regarded as a disturbance. Equation (11) is rewritten as following discrete model:

$$\begin{cases} x(k+1) = A_d x(k) + B_d u(k) + G_d w(k) \\ y(k) = C_d x(k) + v(k) \end{cases} \tag{15}$$

where $v(k)$ is the measurement noise. State variable, control input, uncontrollable disturbance, and output are defined as

$$x(k) \triangleq \begin{bmatrix} p_m(k) & p_f(k) & p_r(k) & \xi_1(k) & \xi_2(k) & \sum_{i=0}^{k} T_s \cdot e(i) \end{bmatrix}^T \tag{16a}$$

$$u(k) \triangleq s_2(k), w(k) \triangleq F_{in}(k), y(k) \triangleq \delta(k), \tag{16b}$$

$$e(k) \triangleq r(k) - y(k) \tag{16c}$$

where $r(k)$ is the tracking reference; and the integration of error between the reference and output is introduced to the state to perform the function of tracking. The discrete cost function is given by

$$J(u) = \sum_{n=0}^{\infty} x^T Q x + u^T R u \tag{17}$$

The associated discrete-time Riccati equation is

$$P(k-1) = {A_d}^T P(k) A_d - {A_d}^T P(k) B_d (P^T B_d P(k) + R)^{-1} {B_d}^T P(k) A_d + Q \tag{18}$$

Through Riccati iteration, the solution of the Riccati equation is represented as $P(\infty)$. The state feedback gain of control law $u = -Kx$ is calculated by

$$K = (R + {B_d}^T P(\infty) B_d)^{-1} {B_d}^T P(\infty) A_d \tag{19}$$

As long as the eigenvalues of $A - BK$ are in the unit circle of z plane, the control method is stable.

3.4. Unscented Kalman Filtering

UKF is developed as an extension of Kalman Filter in nonlinear systems. It is easier to use for nonlinear structural dynamics [28] because it avoids the complicated computation of the nonlinear Jacobian matrix and roundoff error. That is, it is much easier to approximate a probability distribution than an arbitrary nonlinear function. Like Kalman Filtering 5 renewal equations, UKF is divided into five steps, as illustrated in Figure 10.

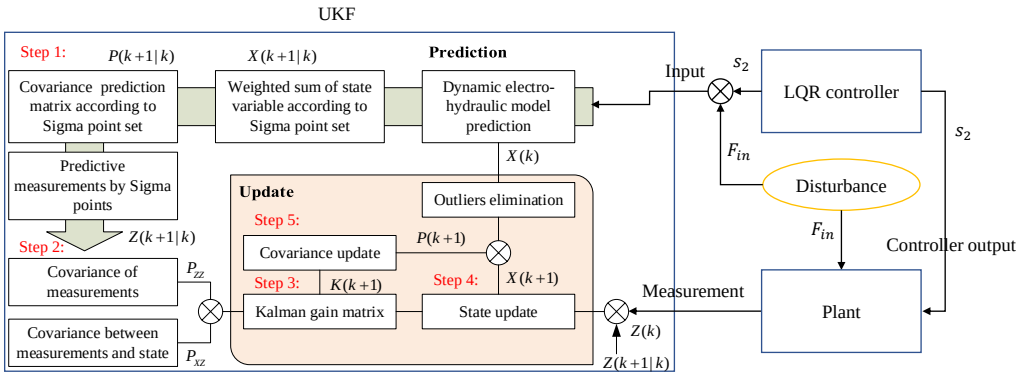

Figure 10. The topology of UKF simulation.

- Step 1: State and measurement are predicted based on state-space through two Unscented Transformation (UT) [29]. The Sigma point set can be used to predict state and covariance:

$$\chi^{(i)}(k+1|k) = f(\chi^{(i)}(k), u(k)) \tag{20a}$$

$$x(k+1|k) = \sum_{i=0}^{2n} \omega_m^{(i)} \chi^{(i)}(k+1|k) \tag{20b}$$

$$P(k+1|k) = \sum_{i=0}^{2n} \left(\omega_c^{(i)} [x(k+1|k) - \chi^{(i)}(k+1|k)] \, [x(k+1|k) - \chi^{(i)}(k+1|k)]^T \right) + Q(k) \tag{20c}$$

where n is the dimension of state vector. $\chi^{(i)}$ is the Sigma point set. $\omega_m^{(i)}$ and $\omega_c^{(i)}$ are the weighting factor aggregate of Sigma points and covariance, and the number of elements in the set is $2n+1$. $Q(k)$ is the covariance matrix of state-space updating error. Then, measurement's prediction is then acquired by a second UT transform aimed at state's prediction:

$$\bar{z}^{(i)}(k+1|k) = h(\bar{\chi}^{(i)}(k+1|k), u(k)) \tag{21a}$$

$$z(k+1|k) = \sum_{i=0}^{2n} \omega_m^{(i)} \bar{z}^{(i)}(k+1|k) \tag{21b}$$

where $\bar{\chi}^{(i)}(k+1|k)$ is the Sigma point set of $x(k+1|k)$;

- Step 2: The internal covariance of the measurement and the cross-variance between measurement and state can be calculated by

$$P_{zz} = \sum_{i=0}^{2n} \left(\omega_c^{(i)} [z(k+1|k) - \bar{z}^{(i)}(k+1|k)] \, [z(k+1|k) - \bar{z}^{(i)}(k+1|k)]^T \right) + R \tag{22a}$$

$$P_{xz} = \sum_{i=0}^{2n} \left(\omega_c^{(i)} [z(k+1|k) - \bar{\chi}^{(i)}(k+1|k)] \, [z(k+1|k) - \bar{z}^{(i)}(k+1|k)]^T \right) \tag{22b}$$

where R is the covariance matrix of measurement error;

- Step 3–5: After the procedure of forecasting, the Kalman gain, the observer's state, and covariance matrix are updated:

$$K = P_{xz} P_{zz}^{-1} \tag{23a}$$

$$x(k+1) = x(k+1|k) + K(z(k) - z(k+1|k)) \tag{23b}$$

$$P(k+1) = P(k+1|k) - K P_{zz} K^T \tag{23c}$$

It is remarkable that the input disturbance is involved in the state space, namely the driver's input force. The driver's intention is assumed to follow the chi-square distribution with N degrees of freedom, which means a higher probability of weak braking conditions than strong braking. The N standard normally distributed noises are also considered the error of the state estimation, plus full-state estimation errors, so there are $N+5$ process noises obeying normal distribution.

It is necessary to tune the noise covariance and the dispersion degree of sigma points appropriately to improve the observation effect of UKF. The tuning effect can be evaluated by a 1σ boundary of the state estimation error covariance matrix. Because UKF is very sensitive to the initial value of the noise covariance and the driver input force perturbation varies over a wide range, the use of adaptive noise covariance often leads to large deviations of the initial computed value from the true value and requires extra time for convergence. In addition, UKF usually introduces algorithms to correct the covariance matrix to ensure the positivity of the covariance matrix. However, the dynamic calculation of the noise matrix will disturb the positivity condition and lead to the impossibility of achieving the Cholesky decomposition.

4. Observation Results of Simulation and Vehicle Test

4.1. Simulation Results

The simulation verification contains the open-loop test and the closed-loop test with the power-assisted controller. The manipulated input is the pushrod displacement s_2, and the disturbance input is the driver's pedal force, which is assumed to follow the chi-square distribution with $n = 1$. The white noise with a covariance of 2.5×10^{-3} is added to the measurement δ in the simulation, while the noises with covariances of 0.25, 0.25, 0.25, 1×10^{-8}, 1×10^{-8} are added to the states to simulate the process error during state prediction. In addition, the Extended Kalman Filter (EKF) is used as the control group to validate the effect of UKF.

In the open-loop test, the pushrod input uses the ramp signal with the slope of 2 mm/s and a simulation period of 10 s, which is enough to cover the majority of the hydraulic nonlinear interval. As shown in Figure 11, two top subfigures are the manipulated input and disturbance input of the system, and the bottom subfigures are the representative states x_2 and x_4 for the comparative performance evaluation. The x_2 observation error of UKF evenly increases with the growth of state. In addition, the behavior of EKF is superior to UKF when x_2 exceeds 2.5 MPa; however, the error of EKF is more than that of UKF when x_2 is under 2.5 MPa, which is influenced by the nonlinear process of the system. The observation effect of UKF for state x_4, which is related to the reaction disk, is better than EKF at all stages.

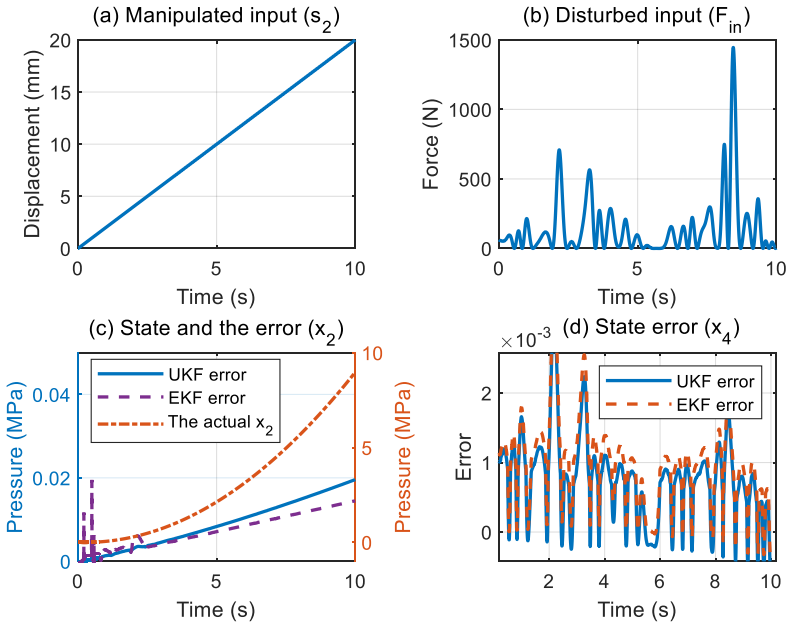

Figure 11. The input and states in the open-loop test.

A comparison of the output variables and the extra measured noise superimposition is shown in Figure 12a. The residual comparison between the two observers is depicted in Figure 12b. The forward process is accompanied by larger residuals, which has no correlation with the noise. The UKF has an improved effect on the residual compared to EKF. The root mean square errors (RMSE) of two observers are displayed in Table 1, and the residual of EKF decreases by 12.75% relatively in the open-loop simulation.

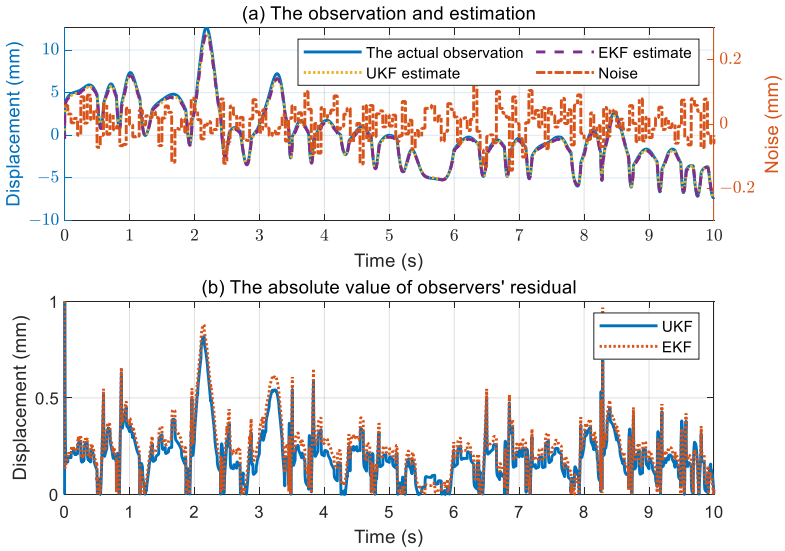

Figure 12. The observation and residual in the open-loop test.

Table 1. RMSE of residual.

Case	EKF	EKF	Improvement/%
Open-loop	0.2758	0.2406	12.75
Closed-loop	0.2405	0.1999	16.87
Vehicle test	0.0565	0.0472	16.47

The input s_2 is decided by the LQR in a closed-loop test to the realize power assistance of the E-Booster. The same pedal force as the open-loop test is used for the disturbance input. In terms of the front chamber pressure x_2 in Figure 13, EKF has18.53% less RMSE than UKF. However, UKF is superior to EKF by 21.44% in terms of the reaction disk state x_4. As shown in Figure 14, the backward process causes a larger observation error in closed-loop simulation. The EKF residual is 16.87% higher than the UKF residual.

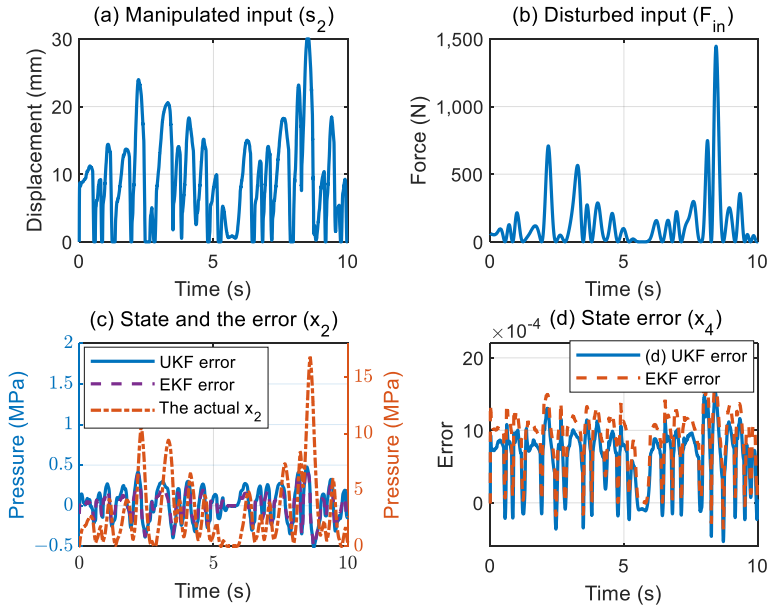

Figure 13. Input and state in closed-loop test.

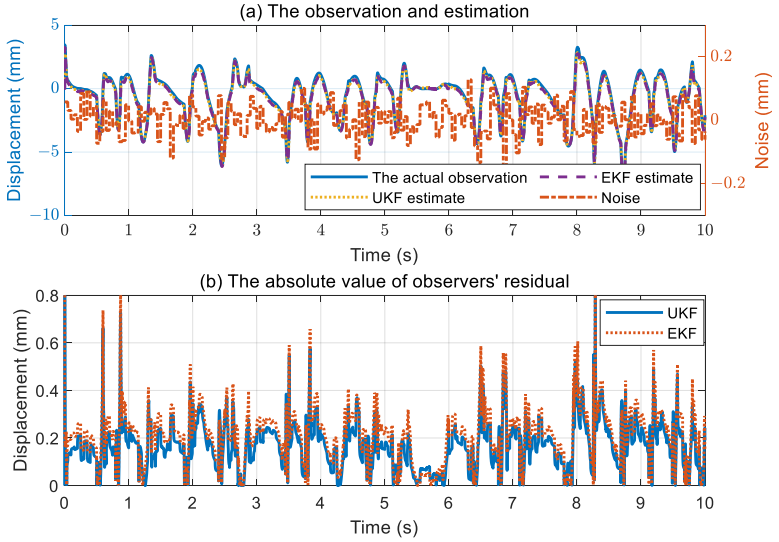

Figure 14. The measurement and its residual in closed-loop test.

Figure 15 displays a comparison of partial states of UKF and 1σ uncertain boundary. The variance σ is updated by the UKF covariance matrix. Those dots of state x_2 and x_4 beyond 1σ boundary account for 2.15% and 7.99%, respectively, which are both less than 30% and almost the same magnitude. It illustrates that the a priori covariance for process error and measurement error is set appropriately.

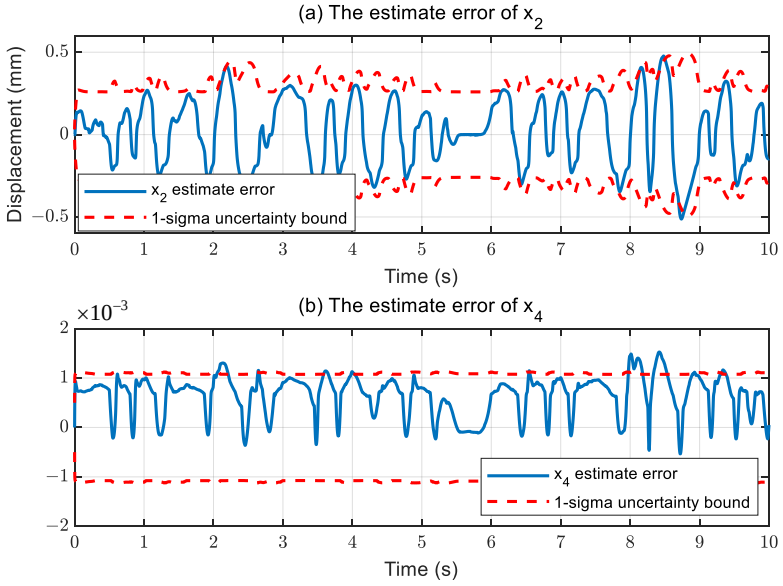

Figure 15. State observation error and uncertain boundary.

4.2. Vehicle Test Results

As shown in Figure 16a, the test vehicle was a sport utility vehicle (SUV). An additional pedal force sensor and master cylinder pressure sensor were added at the brake pedal in order to compare the results. The test road conditions were tarmac (shown in Figure 16b) with a coefficient of adhesion greater than 0.8, which was used to simulate urban roads. The driver performs the braking action according to the road conditions. To cover more braking conditions, the driver randomly enhanced some braking actions.

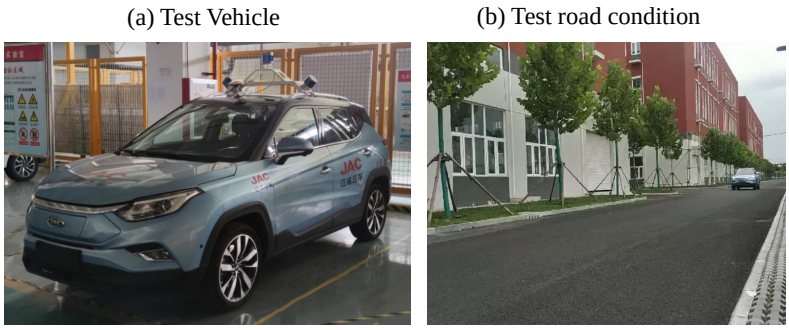

Figure 16. Vehicle test.

Figure 17a,b display the system input, while Figure 17c,d show magnified graphs of the red dotted line in the top subfigures. The observed pressure results of UKF and EKF are consistent with the measurement, but EKF with an RMSE of 0.8750 performs better than UKF with 0.9039. According to Figure 18a,b, which are the output observation and partial magnification box, UKF is closer to the actual value than EKF. Figure 18c,d are the residual comparison between the observers. It is consistent with the simulation results that UKF has 16.47% fewer residuals. As a result, it is concluded that UKF's observation accuracy is better than EKF's.

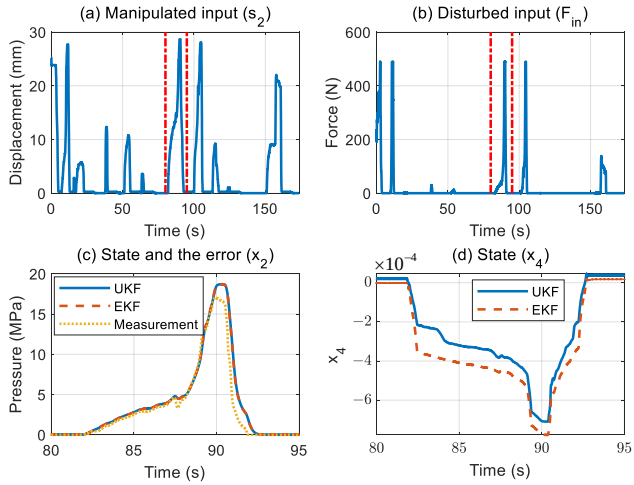

Figure 17. The input and states in vehicle test.

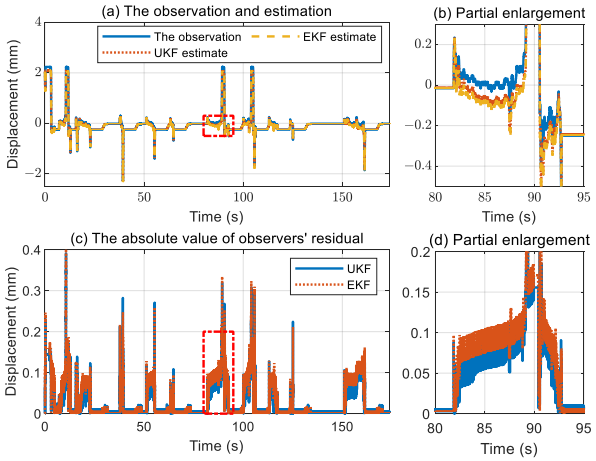

Figure 18. The measurement and its residual in the vehicle test.

5. Conclusions

The proposed UKF observer can realize the observation of all the states with the existence of random disturbance. First, the pre-compression of the reaction disk is designed to guarantee the linear assisted characteristics of E-Booster. Then, the p-V characteristic of the hydraulic system is fitted using the RLS algorithm with the forgetting factor, and the integrated system model is updated with the fitting parameters. In addition, the LQR control method is developed to provide closed-loop tracking of pre-compression under the condition of the driver's input force disturbance. The proposed UKF observer considers the disturbance as a chi-square distribution, and can use the variance of the standard normal distribution to correct the process noise of the observer. Finally, the E-Booster full-state observation is accomplished independent of the master cylinder pressure sensor.

The above method has the following innovative content. At first, this paper fully considers rubber's viscoelastic characteristics and phenomenon of stiffness damage (Mullins effect), and describes them with an empirical formula. Combined with the leverage model, it can well explain the difference between the initial unloaded brake feeling and the subsequent booster feeling. Secondly, to ensure the consistency of all booster processes, this paper proposes a novel pre-compression strategy for the feedback disk, which ensures a constant booster ratio for all processes. To achieve full-state observation of the feedback disk and electro-hydraulic system, a UKF-based observer is subsequently designed. Because the driver's input force disturbance has a large effect, the observer describes the perturbation with multiple Gaussian processes.

Future research will concentrate on the robustness of the closed-loop algorithm, considering the influence of the input force disturbance on the boosting effect, in order to conform as much as possible to the predesigned power-assisted characteristics. The supervised learning approach can also be used to refine the nonlinear hydraulic model, which improves the accuracy of the hydraulic system prediction model and reduces process noise error.

Supplementary Materials: The following supporting information can be downloaded at: https://www.mdpi.com/article/10.3390/act12030094/s1.

Author Contributions: Conceptualization, M.M.; methodology, M.M.; software, M.M.; validation, M.M., S.C. and H.M.; formal analysis, S.C.; investigation, H.M.; resources, L.L.; data curation, Y.P.; writing—original draft preparation, M.M.; writing—review and editing, M.M. and S.C.; visualization, M.M.; supervision, S.C. and L.L.; project administration, L.L.; funding acquisition, L.L. All authors have read and agreed to the published version of the manuscript.

Funding: This research received no external funding.

Data Availability Statement: The data presented in this study are available in supplementary material here.

Conflicts of Interest: The authors declare no conflict of interest. The funders had no role in the design of the study; in the collection, analyses, or interpretation of data; in the writing of the manuscript; or in the decision to publish the results.

Abbreviations

The following abbreviations are used in this manuscript:

E-Booster	Electric brake booster
UKF	Unscented Kalman Filter
EKF	Extended Kalman Filter
KF	Kalman Filter
LQR	Linear quadratic regulator
RLS	Recursive least squares
PMSM	Permanent magnet synchronous motor
GM	Generalized Maxwell
UT	Unscented Transformation
RMSE	Root mean square errors
MPC	Model Predictive Control
SUV	Sport Utility Vehicle

References

1. Todeschini, F.; Corno, M.; Panzani, G.; Fiorenti, S.; Savaresi, S.M. Adaptive cascade control of a brake-by-wire actuator for sport motorcycles. *IEEE/ASME Trans. Mechatron.* **2014**, *20*, 1310–1319. [CrossRef]
2. Todeschini, F.; Formentin, S.; Panzani, G.; Corno, M.; Savaresi, S.M.; Zaccarian, L. Nonlinear pressure control for bbw systems via dead-zone and antiwindup compensation. *IEEE Trans. Control. Syst. Technol.* **2015**, *24*, 1419–1431. [CrossRef]
3. Oshima, T.; Fujiki, N.; Nakao, S.; Kimura, T.; Ohtani, Y.; Ueno, K. Development of an electrically driven intelligent brake system. *SAE Int. J. Passeng. Cars-Mech. Syst.* **2011**, *4*, 399–405. [CrossRef]
4. Xiong, L.; Yuan, B.; Guang, X.; Xu, S. *Analysis and Design of Dual-Motor Electro-Hydraulic Brake System*; SAE Technical Paper; SAE International: Warrendale, PA, USA, 2014.
5. Park, S.; Oh, K.; Jeong, Y.; Yi, K. Model predictive control-based fault detection and reconstruction algorithm for longitudinal control of autonomous driving vehicle using multi-sliding mode observer. *Microsyst. Technol.* **2020**, *26*, 239–264. [CrossRef]
6. Hu, C.; Wei, X.; Ren, Y. Passive fault-tolerant control based on weighted lpv tube-mpc for air-breathing hypersonic vehicles. *Int. J. Control. Autom. Syst.* **2019**, *17*, 1957–1970. [CrossRef]
7. Dai, Y.; Yu, S.; Yan, Y.; Yu, X. An ekf-based fast tube mpc scheme for moving target tracking of a redundant underwater vehicle-manipulator system. *IEEE/ASME Trans. Mechatron.* **2019**, *24*, 2803–2814. [CrossRef]
8. Campos-Delgado, D.U.; Espinoza-Trejo, D.R. An observer-based diagnosis scheme for single and simultaneous open-switch faults in induction motor drives. *IEEE Trans. Ind. Electron.* **2011**, *58*, 671–679. [CrossRef]
9. Diao, S.; Diallo, D.; Laboure, E. A nonlinear observer for dc bus voltage estimation and sensor diagnosis for a battery charger used in automotive systems. In Proceedings of the 2015 IEEE 24th International Symposium on Industrial Electronics (ISIE), Buzios, Brazil, 3–5 June 2015; pp. 438–443.
10. Eng, Y.H.; Teo, K.M.; Chitre, M.; Ng, K.M. Online system identification of an autonomous underwater vehicle via in-field experiments. *IEEE J. Ocean. Eng.* **2016**, *41*, 5–17. [CrossRef]
11. Karras, G.C.; Panos, M.; Bechlioulis, C.P.; Kyriakopoulos, K.J. Unsupervised online system identification for underwater robotic vehicles. *IEEE J. Ocean. Eng.* **2018**, *44*, 642–663. [CrossRef]
12. Ercan, Z.; Carvalho, A.; Gokasan, M.; Borrelli, F. Modeling, identification, and predictive control of a driver steering assistance system. *IEEE Trans. Hum. Mach. Syst.* **2017**, *47*, 700–710. [CrossRef]
13. Cui, Z.; Cui, N.; Wang, C.; Li, C.; Zhang, C. A robust online parameter identification method for lithium-ion battery model under asynchronous sampling and noise interference. *IEEE Trans. Ind. Electron.* **2020**, *68*, 9550–9560. [CrossRef]
14. Mahyuddin, M.N.; Na, J.; Herrmann, G.; Ren, X. Adaptive observer-based parameter estimation with application to road gradient and vehicle mass estimation. *IEEE Trans. Ind. Electron.* **2013**, *61*, 2851–2863. [CrossRef]
15. Nam, K.; Oh, S.; Fujimoto, H.; Hori, Y. Estimation of sideslip and roll angles of electric vehicles using lateral tire force sensors through rls and kalman filter approaches. *IEEE Trans. Ind. Electron.* **2013**, *60*, 988–1000. [CrossRef]
16. Zhou, H.; Liu, Z.; Yang, X. Motor torque fault diagnosis for four wheel independent motor-drive vehicle based on unscented kalman filter. *IEEE Trans. Veh. Technol.* **2018**, *67*, 1969–1976. [CrossRef]
17. Lee, S.; Nakano, K.; Ohori, M. On-board identification of tyre cornering stiffness using dual kalman filter and gps. *Veh. Syst. Dyn.* **2015**, *53*, 437–448. [CrossRef]
18. Boada, B.L.; Garcia-Pozuelo, D.; Boada, M.; Diaz, V. A constrained dual kalman filter based on pdf truncation for estimation of vehicle parameters and road bank angle: Analysis and experimental validation. *IEEE Trans. Intell. Transp. Syst.* **2017**, *18*, 1006–1016. [CrossRef]
19. Calabrese, A.; Strano, S.; Terzo, M. Adaptive constrained unscented kalman filtering for real-time nonlinear structural system identification. *Struct. Control. Health Monit.* **2017**, *25*, e2084. [CrossRef]
20. Jun, H. Modelling and Control of Vehicle Braking System Equipped with Electro-Mechanical Booster. Master's Thesis, Jilin University, Changchun, China, 2018.

21. Lu, L.Y.; Lin, G.L.; Shih, M.H. An experimental study on a generalized maxwell model for nonlinear viscoelastic dampers used in seismic isolation. *Eng. Struct.* **2013**, *34*, 111–123. [CrossRef]
22. Berg, M. A nonlinear rubber spring model for rail vehicle dynamics analysis. *Veh. Syst. Dyn.* **1998**, *30*, 197–212. [CrossRef]
23. Karlsson, F.; Persson, A. Modelling Non-Linear Dynamics of Rubber Bushings-Parameter Identification and Validation. Master's Thesis, Lund University, Lund, Sweden, 2003.
24. Berg, M. A model for rubber springs in the dynamic analysis of rail vehicles. *Proc. Inst. Mech. Eng. Part F J. Rail Rapid Transit* **1997**, *211*, 95–108. [CrossRef]
25. Vollert, H.; Kneip, F.; Mahnkopf, D. Method for Operating a Brake-Boosted Brake System of a Vehicle, and Control Device for a Brake-Boosted Brake System of a Vehicle. U.S. Patent No. 8,886,430, 11 November 2014.
26. Mahnkopf, D. Brake Booster and Method for Operating a Brake Booster. U.S. Patent 9,845,086, 19 December 2017.
27. Coleman, T.F.; Li, Y. An interior trust region approach for nonlinear minimization subject to bounds. *Siam J. Optim.* **1993**, *6*, 418–445. [CrossRef]
28. Mariani, S.; Ghisi, A. Unscented kalman filtering for nonlinear structural dynamics. *Nonlinear Dyn.* **2007**, *49*, 131–150. [CrossRef]
29. Julier, S.; Uhlmann, J.; Durrant-Whyte, H.F. A new method for the nonlinear transformation of means and covariances in filters and estimators. *IEEE Trans. Autom. Control.* **2001**, *45*, 477–482. [CrossRef]